Seismic data acquisition ~~for~~ to ~~combining~~ combine high-resolution seismic reflection and full-waveform inversion – a case study for overdeepened valleys

Thomas Burschil[1], Daniel Köhn[2], Matthias Körbe[3], Gerald Gabriel[3,4], Johannes Großmann[5], Gustav Firla[6], Markus Fiebig[6]

[1]Federal Institute for Geosciences and Natural Resources (BGR), Hannover, 30655, Germany
[2]Kiel University, Kiel, 24118, Germany
[3]LIAG Institute for Applied Geophysics, Hannover, 30655, Germany
[4]Institute of Earth System Sciences, Section Geology, Leibniz University, Hannover, 30655, Germany
[5]Bavarian Environment Agency (LfU), Hof, 95030, Germany
[6]Department of Landscape, Water and Infrastructure, BOKU University, Vienna, 1190, Austria

Correspondence to: Thomas Burschil (thomas.burschil@bgr.de)

Abstract. In the context of the ICDP-project "Drilling Overdeepened Alpine Valleys", the integration of high-resolution seismic reflection (HRSR) and full waveform inversion (FWI) ~~aims~~ is used to enhance detailed near-surface imaging in heterogeneous glacial and post-glacial environments. To meet the specific requirements of both methods, dense P-wave and S-wave datasets were acquired over an overdeepened basin in the northern Alpine foreland, using a combination of vibratory and explosive seismic sources, as well as different receivers. Analysis of the datasets, as well as ~~a~~ separate application of HRSR and FWI demonstrates the suitability of the acquired data. The FWI workflow applied to the P-wave data fits the recorded waveforms and converged successfully, yielding a consistent and physically reasonable model that correlates well with the HRSR images. These datasets are the basis for future methodological development of combining HRSR and FWI.

~~Furthermore,~~The HRSR images reveal important information about the geology of the overdeepened basin near the town ~~of~~ Schäftlarn (Germany). Using standard processing workflows, P-wave HRSR delineates detailed subsurface structures, including the base of the basin, intra-basin discontinuities, and subtle stratigraphic variations. Additional S-wave data provides superior resolution in imaging Quaternary basin sediments down to 200 m depth compared to P-waves and thus offers complementary information.

1 Introduction

Near-surface seismic methods are highly effective in subsurface imaging, particular for ~~example in~~ detecting stratigraphic features and geological discontinuities (Wang et al., 2025). However, seismic imaging ~~i~~In heterogeneous near-surface environments, such as glacial and post-glacial deposits, ~~seismic~~

imaging can beremains challenging (Maraio et al., 2018). Nonetheless, eEven in such complex environments settings, high-resolution seismic reflection method (HRSR) can provides detailed structural information by through the analyzing analysis of the reflected wavefield (e.g., Dehnert et al., 2012; Malehmir et al., 2013; Maries et al., 2017). Depending on the survey parameters, this methodHRSR is capableoften suitable of resolving to image the subsurface structure from depths of only a few metres with a resolution in the sub-metre – with sub-metre resolution – to range down to several kilometres, albeit with with decreasing resolution. The use Utilizing of S-waves, instead of conventionalnient P-waves, can further enhance increase resolution even more (Pugin et al., 2009; Burschil and Buness, 2020; Pertuz and Mahlehmir, 2023). The degree of subsurface complexity largely determines theHowever, the complexity of the subsurface is decisive for the required extent of seismic data processing required to achieve optimalensure best imaging quality. InDepending on the geologically complex settings situation, advanced processing approaches – such as true-amplitude processing using common reflection surfaces or as well as prestack prestack-depth migration – may can be superior to less advanced simpler processing workflows and, thus, reveal undiscovered geological features that remain undetectedare not observable after standard processing. Examples in the context of the investigation of overdeepened structures include are allochthonous Molasse blocks at the base of the sedimentary succession (Burschil et al., 2018) andor cuspate-lobate folding of shallow diamict (Buness et al., 2022).

Full-waveform inversion (FWI) further fertilizes enhances seismic imaging (Tarantola, 1986; Virieux and Operto, 2009) by, enabling a detailed and quantitative reconstruction of subsurface properties (e.g., Operto et al., 2013; Mecking et al., 2021; Singh et al., 2022; Beraus et al., 2024). In addition, eWith elastic FWI additionally allows for the is able to estimatione, it is possible to gain information about of S-wave velocities from P-wave data as well (Pan et al., 2019; Roodaki et al., 2024). However, Bboth methods, however, have their limitations. : HRSR relies on impedance contrasts and shallow reflections may be superimposed masked by near-surface scattering (Frei et al., 2015; Sloan et al., 2016). In contrast, while FWI is computationally demandingintensive (Ren and Liu, 2015) and its success depends strongly on high-quality field data and accurate initial models, including both P- and S-wave velocity distributions (Vigh et al., 2018; Zhang et al., 2025).highly sensitive to initial model accuracy (Zhang et al., 2025). The applicability of the latter depends heavily on high-quality field data and initial models (Vigh et al., 2018). For elastic FWI, this includes initial P-wave and S-wave models. Despite these challenges, we expect that their combining HRSR and FWIed has the potential to application significantly improves geophysical interpretations in near-surface imaging, yielding investigations, leading to better higher resolution, accuracy, and interpretational reliability in data analysis. The two approaches HRSR and FWI set impose different requirements on the raw acquired data. HRSR benefits needs from a broad bandwidth of the source signal to producegain sharp reflections (Brodic et al., 2021), whereas s. State-of-the-art FWI workflows iteratively invert the data iteratively in multiple stages, starting fromwith a low frequency band to avoid cycle skipping (Dokter et al., 2017; Vigh et al., 2018; Köhn et al., 2019). These complementary demandsprerequisites make the design of cause field-data acquisition challenging, when aiming for an integrated application of both methodses for the acquisition of field data that is to be analyzed by an integrated approach.

To overcome these challenges, a variety of ~~different~~ land seismic sources ~~are available~~can be used, e~~.~~ ~~E~~ach with distinct ~~of them has certain~~ advantages and disadvantages in generating~~emitting~~ seismic waves. Vibratory sources are ~~often~~ frequently used because~~since~~ they provide highly repeatable ~~the~~ signals and ~~is highly repeatable and the vibrators~~ emit ~~the~~ energy over an extended~~certain~~ time period~~length~~. While ~~Th~~the total emitted energy accumulates, the ~~but the~~ instantaneous emitted energy released at any moment remains low, minimizing ground impact ~~is low so that the impact on the ground is low~~ and preventing damage to land or infrastructure ~~is avoided~~. The high repeatability of signals with ~~ability of emitting the same signal with~~ identical~~the same~~ frequency content is particularly beneficial for vertical stacking, as it improves signal coherency and reduces random noise~~high~~ (Brodic et al., 2021) ~~and advantageous for vertical stacking to reduce incoherent noise~~. The peak force of a seismic vibrator refers to the maximum force exerted~~output that the vibrator can exert~~ on the ground during operation (Sallas, 1984). The emitted sweep signal, defined by ~~with a defined~~ its frequency band, is correlated with the recorded traces, ~~and~~ produc~~ing~~es a zero-phase Klauder-wavelet ~~by correlation with itself~~ through self-correlation (Lines and Clayton, 1977). ~~Depending on the frequency band and the ground coupling, the emitted signal is close to the ideal, sharp Klauder-wavelet.~~ In addition to these ~~Both~~ technical benefits, ~~advantages are complemented by~~ vibrators are often preferred for economic reasons, fewer regulatory constraints~~ions~~, and ease of approval. However, ~~seismic vibrators~~ they are technically ~~-~~limited ~~in generating~~in that they cannot generate ~~exciting~~ low~~-~~-frequency signals~~ies~~ (Wei and Phillips, 2011). In contrast, impulsive sources ~~emit~~ release~~the~~ seismic energy instantaneously and ~~.~~ ~~These sources~~ often contain ~~more a~~ low frequency components. Yet, the achievable ~~content, but depending on the emitted energy of the source, the depth of seismic~~ imaging depth depends on the total emitted energy~~is limited~~. ~~Commonly~~ Commonly-used impulsive sources are sledgehammers, drop weights, and explosives with variable~~ous~~ charge sizes. While sledgehammers and drop weights result in limited penetration depth, explosives, deployed in boreholes, ~~can be~~are used for shallow and deep imaging~~penetration~~ (Denny and Johnson, 1991). Nevertheless~~However~~, the use of~~using~~ explosive source~~s~~ is restricted~~not possible everywhere~~in certain environments, such as~~for example in~~ urban areas.

On the receiver side, geophones have been used since the early 20th ~~century~~ Century to record ~~the~~ ground motion (Dragoset, 2005). Their sensitivity decreases toward lower frequencies, d~~D~~epending on the damping and ~~, the~~ resonance frequency ~~gives a decreasing sensitivity for lower frequencies~~ of the sensor (Krohn, 1984). Cabled systems allow~~enable~~ a direct monitoring~~control~~ of ~~the~~ ground motion and, consequently~~thus~~, immediate quality control during acquisition. In recent years, a~~A~~utonomous recording systems have become increasingly affordable and reliable, making it possible to ~~stable so that~~ maintain a high fold, even if ~~the failure or loss of~~ a few percent of receivers fail or are lost ~~still enables a high fold~~ (e.g., Manning et al., 2019; Ourabah and Chatenay, 2022).

To ~~gain~~ obtain suitable~~adequate~~ datasets for the methodological development of combining HRSR and FWI, we acquired field data using various~~with different~~ source-receiver combinations. E~~We use~~ explosive sources were employed to generate~~excite~~ low frequencies, whereas ~~and~~ vertical vibrator~~s~~ ~~sources~~ provided signals with ~~for a signal with~~ a broad bandwidth. ~~Densely~~ Densely-spaced vertical geophones recorded the ground motion, while a~~. A~~dditional autonomous three~~3~~-component geophones with ~~a~~ lower resonance frequenc~~ies~~ and sparser spacing captured~~receive~~ the low~~-~~-frequency content ~~of~~

~~the ground motion~~. ~~Horizontally~~ Horizontally-oriented vibrators and receivers complement the dataset, supplying ~~to provide~~ the initial S-wave velocity model~~s~~ for FWI.

The first objective of this ~~paper~~ study is to present the acquired field datasets and demonstrate ~~show~~ that the~~y~~ese meet the requirements~~prerequisites~~ for both~~of~~ HRSR and FWI. The r~~R~~esults obtained from separately processed datasets – H~~of each method, processed separately (H~~RSR using P-~~wave~~ and S-wave, and ~~as well as~~ FWI – p~~), p~~rovide insights into the ~~acquired~~ data quality~~sets~~ and confirm~~demonstrate~~ their ~~that they are~~ suitabilit~~yle~~ for future methodological development, ~~of~~ combining both approaches for imaging ~~HRSR and FWI for~~ overdeepened valleys. The second objective ~~of this paper~~ is to image the structure of an overdeepened basin near~~, close to~~ the town ~~of~~ Schäftlarn (Germany). The study area lies~~is located~~ in the Alpine foreland, approximately ~~about~~ 30 km south of Munich, and ~~forms. It and~~ is part of a complex system of overdeepened valleys and basins that are wide~~ly~~ spread across the European Alps (Preusser et al., 2010). It is ~~and one~~ also one of the study sites of the ICDP project, *Drilling Overdeepened Alpine Valleys* (DOVE).

2 The DOVE project and study site Schäftlarn

The ICDP project *Drilling Overdeepened Alpine Valleys* (Anselmetti et al., 2022) investigates ~~glacially~~ glacially-overdeepened structures on a pan-Alpine basis using drill cores and geophysical surveys. The pinpoint information gained by the cores is extrapolated by the geophysical surveys into 2-D and 3-D. Previous investigations ~~focusing~~ focused on overdeepened structures were limited to ~~a~~ local/regional scope. DOVE aims to gather a comprehensive picture of overdeepened structures on the scale of a whole mountain range. The core research questions to be investigated revolve around the timing and extent of Middle Pleistocene glaciations and the sedimentary dynamics associated with them.

Glacial erosion sculpted not only the high Alpine regions but also the foreland. The study site is located in the northern Alpine foreland that was influenced by repeated Pleistocene glaciations (Preusser et al., 2010). About 30 km south of Munich (Germany), the former Isar-Loisach glacier lobe excavated an overdeepened basin, which Jerz (1979) described as a branch basin of the Wolfratshausen Basin to the south. The overdeepened basin is located at the morphologically defined ice-marginal position of the Last Glacial Maximum (LGM; Fig. 1a). The local bedrock consists of Upper-Freshwater Molasse sediments and the basin is filled with Quaternary sediments. To the west of the study site, Lake Starnberg and Lake Ammersee provide examples of overdeepened basins that are not entirely filled by sediments. The study site is located on the southern margin of the Munich gravel plain ("Münchner Schotterebene"; Jerz, 1993). The western area of the study site is elevated approximately 100 m above the recent incision of the Isar valley ~~in~~ to the east (Fig. 1b). The Molasse bedrock has been identified in outcrops at the base of the Isar valley slope (Jerz, 1987).

At the DOVE site Schäftlarn (ICDP site 5068_3), the Bavarian Environment Agency drilled a research borehole (5068_–3_–A) in 2017 and conducted a seismic refraction survey in 2018. The 198.8 m long drill-core (Fig. 1c) shows the sedimentary sequence from bottom to top: (A_1/A_2) ~83 m of fine-grained

sediments, (B) ~111 m of coarse-grained sediments, and (C) ~4 m of diamictic sediments. Remnants of a basal diamict were recovered, but the bedrock was not reached (Firla et al., ~~submitted~~2024). The refraction survey did not image beneath the coarse-grained sediments.

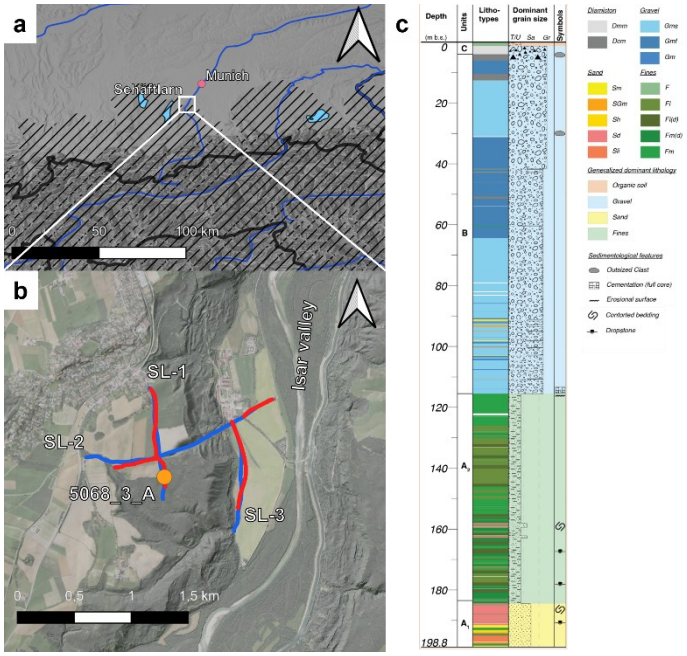

Figure 1: Study area. (a) Overview map showing the location at the margin of the LGM ice extent (hashed area; Ehlers et al., 2011) and (b) location map with borehole ICDP 5068_3_A (orange) and seismic P-wave (blue) and S-wave (red) profiles. (c) Core description of borehole 5068_3_A after Firla et al. (~~submitted~~2024).

3 Data acquisition

At the study site, ~~we acquired data along~~ three seismic profiles (SL-1 to SL-3) were acquired using both P-~~waves~~ and S-waves (Tab. 1; Fig. 1b). The layout was ~~chosen~~ designed to image the internal basin structure~~inventory~~ as well as its base, which is estimated to lie approximately ~~at ca.~~ 200 m below the surface. For each seismic ~~profile~~line, ~~we appended~~ an additional suffix ~~to~~ indicates the wave type: 'P' for P-waves and 'S' for S-waves (e.g. ~~for example~~ SL-1P ~~for the P-wave section~~ and SL-1S ~~for the S-wave section~~). Profile SL-2S ~~is~~ consists of two ~~-~~parts,~~ed~~ because the central section ~~since the central part~~ of SL-2 was in~~not~~ accessible for the S-wave survey.

Table 1: Specifications of seismic profiles, including the number of vibrator ~~points~~ (VP) and explosive ~~, shot points~~ (SP) shot points~~of explosive sources~~, and receiver points (RP).

	P-wave						S-wave				
Profile	length	# of VP	VP spacing	# of SP	# of RP	RP spacing	length	# of VP	VP spacing	# of RP	RP spacing

SL-1	1020 m	211	5 m	9	408	2.5 m	960 m	250	4 m	408	1m
SL-2	1835 m	331		11	468		580 m	149		579	
							300 m	81		299	
SL-3	1020 m	210		5	408		800 m	208		408	

3.1 Seismic sources

To excite generate P-waves, we used employed the 4-ton hydraulically driven vibrator MHV4P (Fig. 2a) from of the LIAG Institute for Applied Geophysics, which has a vertical shaking unit (Burschil et al., 2021). This vibrator has a peak force of 30 kN and is limited to a lowest minimum frequency of 20 Hz. In areas inaccessible that were not accessible to vehicles, such as (the central part of SL-2PP), we used the electrodynamic vibrator ELVIS-7 (Wadas et al., 2016) with a vertical shaking unit was used (Fig. 2b). This wheelbarrow-mounted source, with a 1 kN peak force, can also be deployed along challenging difficult paths. For both sources, we set a dense vibrator point spacing of (5 m)was applied, which corresponds towas doubled twice the receiver spacing of (2.5 m) along the profile. This configurationspacing has been shownproven to be effective to be efficient for shallow investigations in previous studies (e.g., Tanner et al., 2015; Wadas et al., 2016; Burschil et al., 2018). A 12-s sweep with linearly increasing frequencies of 20-200 Hz was used. In addition, we were able to conduct explosive sources ons using with a total of 1 kg charges per shot point were deployed location (Fig. 2c, d), deployed in four 2-m deep boreholes per shot point location (Figs. 2c, d). Boreholes were created by pushing aA hydraulic breaker on a mid-sized excavator was used to push a 2-meter-long metal rod into the ground with a hydraulic breaker mounted on a mid-sized excavatorto create the boreholes. We used aA 1 x 1 m metal plate with a 1-by-1-m jig was used for positioning. Due to logistical and financial constraints, For the entire acquisition, only 26 explosive source shot points were feasible due to logistic and financial constraints. For S-wave excitation, As an S-wave source, we used the ELVIS-7 vibrator with a horizontally oriented shaking unit, positioned perpendicular to the profile direction, was used. The nominal vibrator point spacing was 4 m (four times the receiver spacing of 1 m), which represents a was a compromise betweenregarding the fold and the measuring efficiencyprocess. A 12-s linear sweep with frequencies of 20-120 Hz was appliedused for the S-wave surveys.

Figure 2: Seismic sources. (a) Vibrators MHV4P, (b) ELVIS-7, (c) explosive charge, and (d) boreholes prepared for charging.

3.2 Recording, receivers, and layout

For the P-wave surveys, 17 Geometric Geodes with 24 channels each were used for recording (Tab. 2). As receivers, ~~we deployed~~ 408 vertical single-component 20-Hz geophones were deployed and connected via cable to the Geodes (Fig. 3a). ~~The geophones are connected via cable to the Geodes.~~ Each Geode correlated the signal using a pilot sweep and transferred the digitized data to the recording vehicle via a wired network. The nominal receiver spacing was 2.5 m, ~~to~~ ensuring ~~a good~~dense coverage and ~~to achieve~~ a CMP bin size of <2.5 m to avoid spatial aliasing (cf. Buness et al., 2022). ~~For the layout, we chose~~A ~~a~~ single spread layout was applied for SL-1P and SL-3P, whereas~~.~~ ~~For profile SL-2P, we used~~ a split-spread layout with roll-along geometry was used for SL-2P. The roll-along distance was chosen such that the maximum offset was ~~at least~~ sufficient to image the expected basin depth of approximately ~200 m (cf. Burschil, 2024 for more details).

In addition, ~~for the P-wave survey, we deployed~~ 28 autonomous Omnirecs DATA-CUBE^3 ~~recording~~ units were deployed along the P-wave profiles (Fig. 3b). ~~Three-component 4.5-Hz geophones~~ Each unit was~~ere~~ connected to a three-component 4.~~-~~5 Hz geophone ~~each DATA-CUBE³. These receivers were intended to detect~~ to record lower frequencies more efficiently than the 20-Hz geophones ~~more effectively~~. The DATA-CUBE^3 ~~se~~ receivers~~geophones~~ were placed at ~~approximately~~ 40-60 m intervals in a ~~spacing as a~~ single~~-~~-spread configuration.

For the S-wave survey, ~~we used~~ 10 Geometric Geodes were connected to two landstreamers for recording (Fig. 3c). Each landstreamer consisted~~s~~ of 120 horizontal 10-Hz geophones with 1 m spacing, ~~recording~~ oriented~~ground motion~~ perpendicular to the profile direction. ~~For the layout, we used~~A ~~a~~ split-spread roll-along ~~layout with roll-along~~ geometry, as used in previous surveys (Burschil and Buness, 2020), was applied.

We refer to these datasets on the receiver side as geode-data, cube-data, and landstreamer-data, respectively.

Table 2: Specifications of seismic receivers.

	Recording	Geophones	Orientation	# of channels	Nominal spacing	Mode
geode-data	Geometrics Geode	Sensor SM-6, 20 Hz	vertical	408	2.5 m	triggered
cube-data	DATA-CUBE^3	HL-6B, 4.5 Hz	3-component	3x 28	~40-60 m	autonomous
landstreamer-data	Geometrics Geode	Sensor SM-6, 10 Hz	horizontal	240	1 m	triggered

Figure 3: Seismic receivers. (a) Planted vertical geophones connected by cable, (b) 3-component geophone and DATA-CUBE³, and (c) landstreamer with horizontal geophones.

4 Data processing

To date, HRSR processing and FWI were performed for different datasets ~~so far~~ (Tab. 3). In a future step, ~~The~~ the cube-data will contribute to combining HRSR and FWI ~~in a future step~~.

Table 3: Processing of different datasets. The cube-data are not processed yet.

		Source		
		Explosives	Vertical vibrators	Horizontal vibrator
Receiver	geode-data	FWI	HRSR	
	cube-data	X	X	
	landstreamer-data			HRSR

4.1 HRSR processing

P-wave data were~~seismic~~ process~~ed~~ing ~~was carried out~~ using Landmark ProMAX/SeisSpace ~~Version 5000.11.0.0~~. ~~For all profiles, we used the~~The same processing workflow and parameters were applied to all profiles,~~ following previous studies (e.g., Dehnert et al., 2012; Burschil et al., 2018). The workflow~~ comprise~~d~~ing several processing steps, as summarized in ~~(~~Table~~.~~ 4~~)~~. Step P5a was ~~only~~ applied only to profile SL-2P. The combination of elevation static correction and residual statics ~~worked~~ proved sufficient~~ly~~ so that no refraction static correction was required~~needed~~. Step P10 yielded ~~provides~~ a stacking velocity field ~~for~~ every 25th CMP, which was subsequently ~~that we~~ converted and adapted for migration (step P17) and time-to-depth conversion (step P20).

Table 4: Seismic P-wave processing steps.

Processing step		Parameter
P1	Trace editing	

P2	Vertical stacking for noise suppression	
P3	Geometry assignment	CMP spacing 1.25 m
P4	True amplitude recovery	spherical divergence correction with 1-D velocity distribution
P5	Minimum phase transformation	with adapted wavelet
P5a	Match filtering between MHV4P and ELVIS-7 source	for SL-2P only
P6	Surface consistent spike deconvolution	type: spike, operator length 140 ms
P7	Adaptive deconvolution (L2 norm spiking)	type: spike, operator length 80 ms
P8	F-K filtering for near offsets	-100 m – 100 m, to eliminate chevron patterns
P9	Elevation static correction	datum 680 m, correction velocity 1400 m/s
P10	Two iterations of velocity analysis in combination with residual statics	Every 25th CMP
P11	Automatic gain control	250 ms window length
P12	Normal moveout correction	40 % stretch mute
P13	Common-midpoint stacking	shift to final datum
P14	Bandpass filtering	Ormsby filter, 50-60-170-190 Hz
P15	F-X deconvolution	80 ms window length, 40-450 Hz
P16	Automatic gain control	500 ms window length
P17	Poststack FD time migration	angle <45°
P18	Bandpass filtering	Ormsby filter, 50-60-170-190 Hz
P19	Automatic gain control	500 ms window length
P20	Time-to-depth conversion	smoothed velocity field

S-wave processing of horizontal-vibrator and landstreamer-data was adapted from the ~~processing~~ workflow ~~discussed~~ described in Burschil and Buness (2020) and carried out using Shearwater Reveal ~~Version 6.2~~. The same ~~workflow~~ processing sequence was applied~~used~~ to ~~for~~ all profiles, ~~and~~ the individual ~~. The processing s~~steps are summarized in Table 5. Step S9~~8~~ provide~~sd~~ the stacking velocities, which were analyzed at intervals of at least ~~every~~ 50 m, then ~~and subsequently~~ smoothed and converted to interval velocities using the Dix equation (Sheriff and Geldart, 1995). For step S10, a 200% stretch mute was applied during NMO correction to account for the low velocities of the S-waves. Migration was omitted to~~For S-wave processing,~~ avoid ~~we waived migration to reduce~~ migration artifacts.

Table 5: Seismic S-wave processing steps.

Processing step		Parameter
S1	Trace editing	
S2	Vertical stacking	
S3	Geometry assignment	CMP spacing 0.5 m

S4	Surface-consistent corrections	in the source and receiver domains
S5	Surface-consistent deconvolution	for sources and receivers
S6	Bandpass filtering	time-variant Butterworth filter <400 ms: 50-60-100-120 Hz >400 ms: 30-40-100-120 Hz
S7	Automatic gain control	200 ms window length
S8	Apply residual statics using brute stack	
S9	Several iterations of velocity analysis at a floating datum	guided by reflectors in the stacked section
S10	Normal moveout correction at floating datum	200% stretch mute
S11	Common midpoint stacking	shift to final datum
S12	Automatic gain control	200 ms window length

4.2 Full waveform-inversion

For FWI, ~~we used~~ the latest version of DENISE Black Edition (Köhn et al., 2012; 2014) was used. This multiparameter FWI simultaneously optimize~~ss~~ the P-~~wave~~ and S-wave velocities as well as the density ~~simultaneously~~, ~~using~~ employing adjoint state gradients within the L-BFGS optimization method (Liu and Nocedal, 1989). As input data for the first FWI, we used the geode-data from the explosive sources. The raw data were preprocessed ~~by~~ with a~~using a~~ 30-Hz ~~low~~high-cut filter. ~~As~~ T~~t~~he initial P-wave model was constructed ~~, we created~~ as a 1-D gradient model based on first-~~-~~arrival analysis. The initial S-wave velocity model v_S was~~is~~ estimated from the P-wave velocities v_P using the relation~~by the following equation~~:

$$v_S = \frac{v_P}{\sqrt{3}}. \quad (1)$$

The initial density ~~initial~~ model ρ is ~~estimated~~ derived from~~by~~ the empirical relation by (Ulugergerli and Uyanik (~~,~~2007)~~:~~:

$$\rho = 1000 * (0.1055 * \log(v_S) + 1.3871). \quad (2)$$

~~From a~~Analysis~~zing~~ of the Rayleigh surface waves, compared to the P-wave first arrivals, revealed ~~we inferred~~ a significant influence of damping, so that ~~we chose~~ a visco-elastic modelling approach was adopted. To mitigate the non-linearity of the inverse problem, a sequential ~~frequency~~ inversion ~~approach is applied~~was performed~~. The FWI workflow consists of a sequential frequency approach,~~, inverting field data in frequency bands up to 7 Hz, 10 Hz, 15 Hz, 20 Hz, 25 Hz, and 30 Hz, ~~respectively~~in this order. The source wavelet for each source gather ~~is~~ was ~~computed~~ estimated by a stabilized Wiener deconvolution. An anisotropic, spatial 2-D Gaussian filter imposed smoothness constraints on the adjoint state gradients; its length was scaled to the local P- and S-wavelengths,

applied 1x the local wavelength in ~~Smoothness constraints are imposed by an anisotropic, spatial 2-D Gaussian filter, whose length is adapted to the local P-/S-wavelength, and which is applied to the adjoint state gradients, respectively. In~~ the x-direction and ~~, the gradients are smoothed over 1x local wavelength, and in the y-direction over~~ 0.5x in the y-direction~~the local wavelength~~. Parameter cross-talk ~~is~~ was mitigated by using quasi-Newton L-BFGS optimization ~~together~~ with parameter scaling, where ~~the~~ density updates ~~are~~ were reduced~~systematically decreased~~ by a factor of 0.5~~x~~ compared to the ~~seismic~~ velocity ~~model~~ updates. Finally, a global correlation norm ~~is~~ was employed~~used~~ as an objective function to minimize ~~mitigate~~ source-receiver coupling effects.

5 Results

5.1 Field data and spectral composition

The acquired data exhibit~~show exhibit is an~~ excellent quality ~~data~~ across all ~~quality on the various~~ source and receiver configuration~~setting~~s (Fig. 4). Explosive sources ~~have~~ provided strong ~~a good~~ground coupling and sufficient penetration depth. The dense receiver spacing of the geode-data ~~provide~~ ensures ~~a clear~~distinct first P-wave arrival~~, essential for the generation of an initial P-wave model for FWI~~ (red arrows in Fig. 4), which is essential ~~for~~to construct~~ing~~ the initial P-wave model for FWI. In contrast, t~~T~~he explosive data show strong surface waves, which appear ~~that are~~ aliased in the sparsely space~~ding~~ ~~of the~~ cube-data (blue arrows). The MHV4P vibrator source ~~MHV4P generated~~ produced ~~excellent~~ high-quality reflections (~~yellow~~ orange arrows) and generated less surface waves than the explosive source data. ~~An~~ A~~a~~ir wave ~~arrival~~ noise is also visible in the data (green arrow).

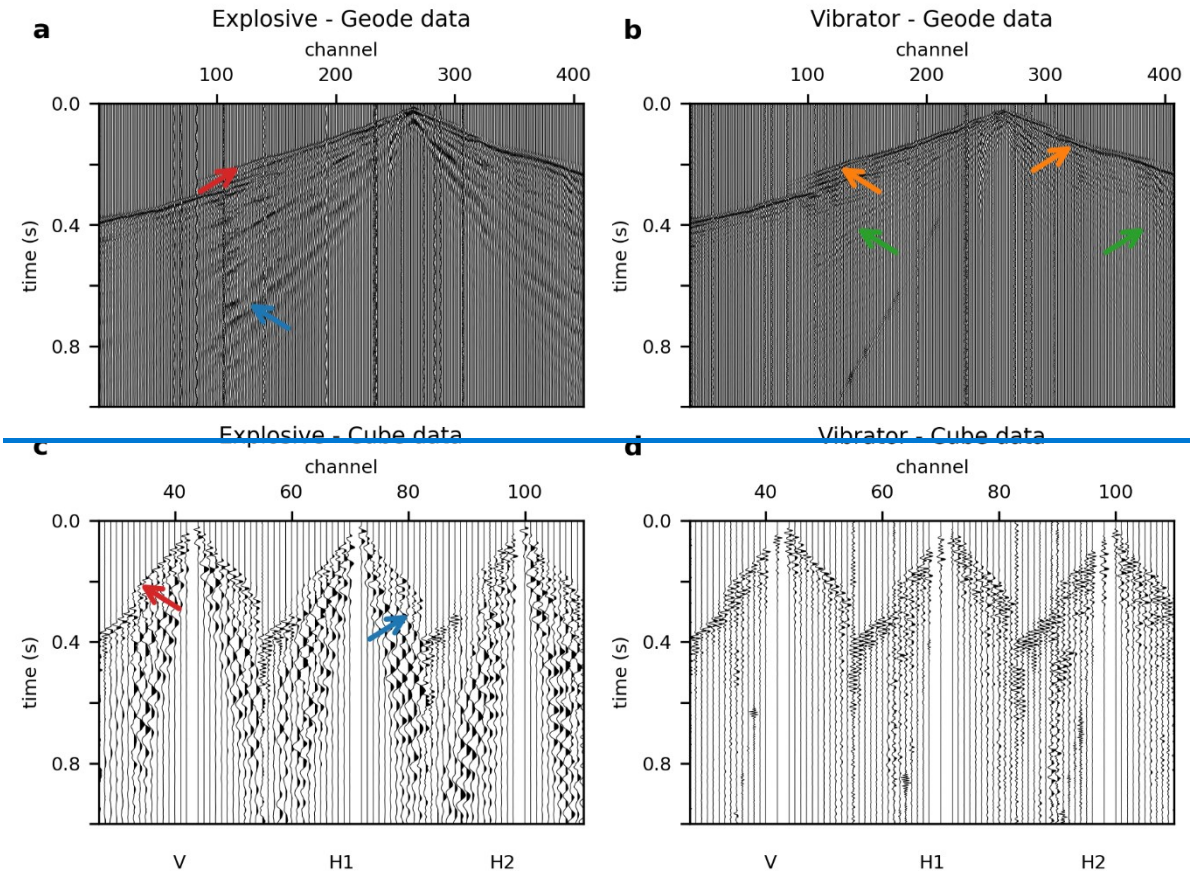
a
Explosive - Geode data
channel
100
200
300
400
0.0
0.4
0.8
time (s)
b
Vibrator - Geode data
channel
100
200
300
400
0.0
0.4
0.8
time (s)
c
Explosive - Cube data
channel
40
60
80
100
0.0
0.4
0.8
time (s)
V
H1
H2
d
Vibrator - Cube data
channel
40
60
80
100
0.0
0.4
0.8
time (s)
V
H1
H2

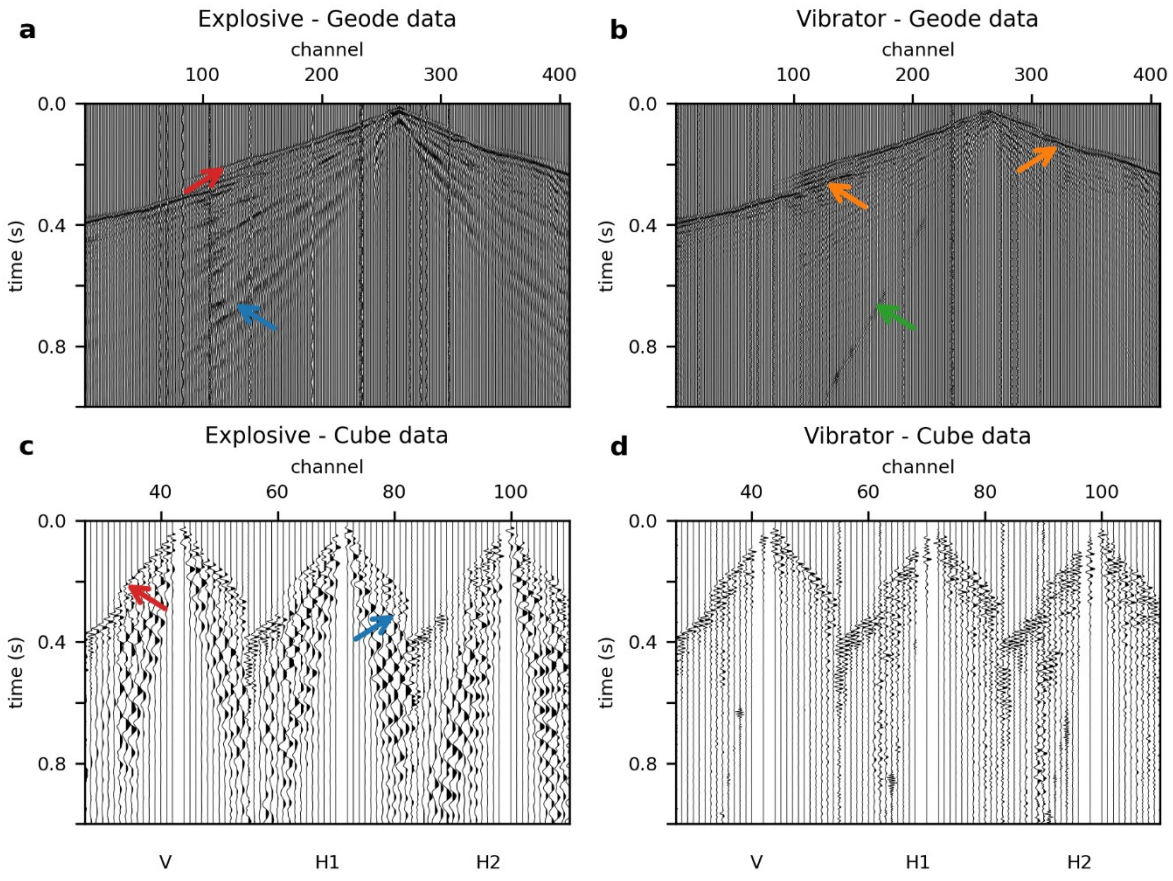

Figure 4: Records for one source location (corresponding power spectral density in Fig. 5). (a) Explosive source and geode-data (20 Hz geophones), (b) vibratory source and geode-data (20 Hz geophones), (c) explosive source and cube-data (3-component 4.5 Hz geophones), (d) vibratory source and cube-data (3-component 4.5 Hz geophones). Note the strong surface waves (blue arrows) and the clear first arrivals (red arrows) in the explosive data, the high frequency reflections (orange arrows) in the vibratory data, as well as the air blast (green arrows).

The frequency content of the P-wave data varies ~~across~~ among the different source-receiver configurations (Fig. 5). The ~~data of the~~ vibrator~~-~~ source ~~and~~ geode-data (20 Hz geophones) ~~show~~ display the ~~entire~~ full sweep frequency range of 20-200 Hz. The corresponding cube-data (4.5 Hz geophones) ~~show~~ reproduce the same lower frequency ramp ~~as the geode-data,~~ but exhibit ~~a~~a high~~-~~frequency ~~cut~~cut-off ~~frequency~~ ~~around~~ near 160 Hz. This limitation arises from a built-in anti-alias filter of the ~~The~~ DATA-CUBE^3~~-~~, which operates at approximately ~~have a maximum time sampling of 2.5 ms (400 Hz). The cut-off of higher frequencies is due to an anti-alias filter in the device at~~ 80% of the Nyquist frequency (160 Hz; T. Ryberg, priv. comm.), given by the maximum sampling interval of 2.5 ms (400 Hz). For the explosive sources, ~~we detect a~~ frequenciesy ~~content~~ below 20 Hz are clearly observed in all datasets. Even the geode-data with 20 Hz geophones contain~~show~~ a significant amount~~portion~~ of energy below their nominal resonance frequency, showing a ~~20 Hz, the~~ low~~-er~~ frequency spectrum similar to~~flank looks similar to~~ the cube-data ~~with 4.5 Hz geophones~~. However, the

baseline level at these frequencies is considerably lower for the cubed data ~~at these low frequencies the base level of the cube-data is much lower~~ than for the geode-data.

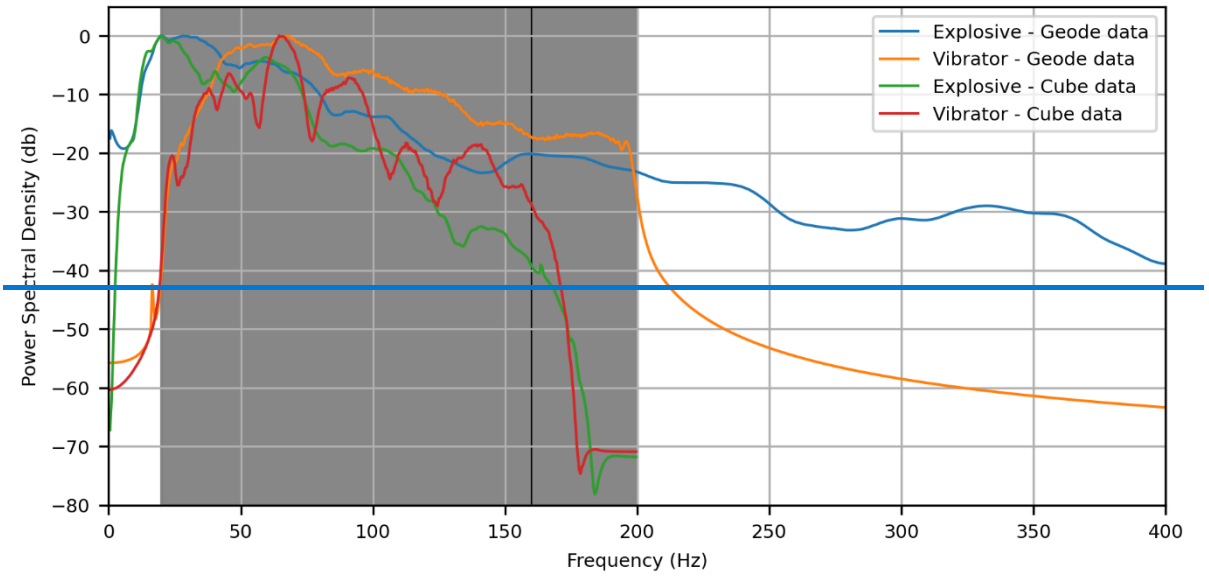

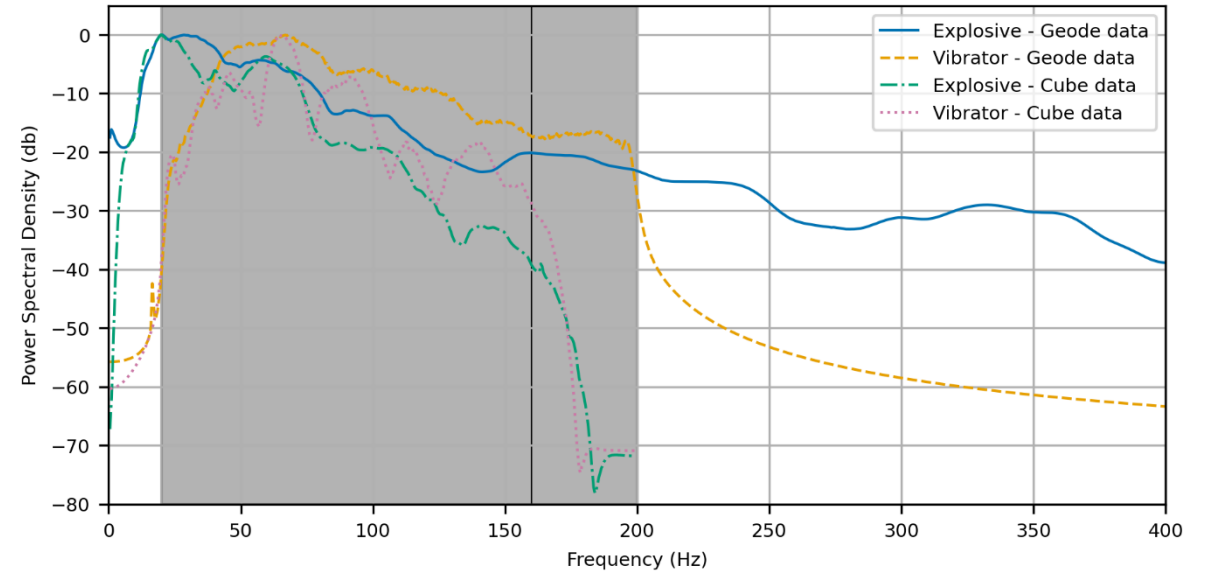

Figure 5: Power spectral density for one record at profile SL-1P (corresponding record in Fig. 4). Explosive source and 20 Hz geophones (blue solid line), vibratory source MHV4P and 20 Hz geophones (orange dashed line), explosive source and vertical component of 4.5 Hz geophones (green dash-dotted line), vibratory source and vertical component of 4.5 Hz geophones (red dotted line). The sweep frequency range is shaded (gray).

In~~A~~t the central part of profile SL-2P, we ~~had to~~ used ELVIS-7 ~~as the vibrator~~ vibrator source~~. The ELVIS-7 source~~ (peak force of ~1 kN) that emitted~~s~~ substantially less energy than the 4-ton hydraulic

vibrator MHV4P (peak force of 30 kN) ~~emits~~, which can ~~clearly~~directly be observed clearly in the data (Fig. 6). While ~~the~~ first arrivals from the MHV4P can be clearly traced across~~along~~ the entire receiver spread ~~for MHV4P~~ (blue arrows in Fig. 6), thos~~e first arrivals from of the vibrator~~ ELVIS-7 are only visible at~~for~~ offsets below ~~<~~250 m (orange arrows). The emitted energy of the ELVIS-7 source is less than the energy of the MHV4P, as we directly observe in the data. ~~However~~Nevertheless, both sources produce~~show~~ d a frequency content for the entire sweep from 20-200 Hz above the background noise level (Fig. 6c).

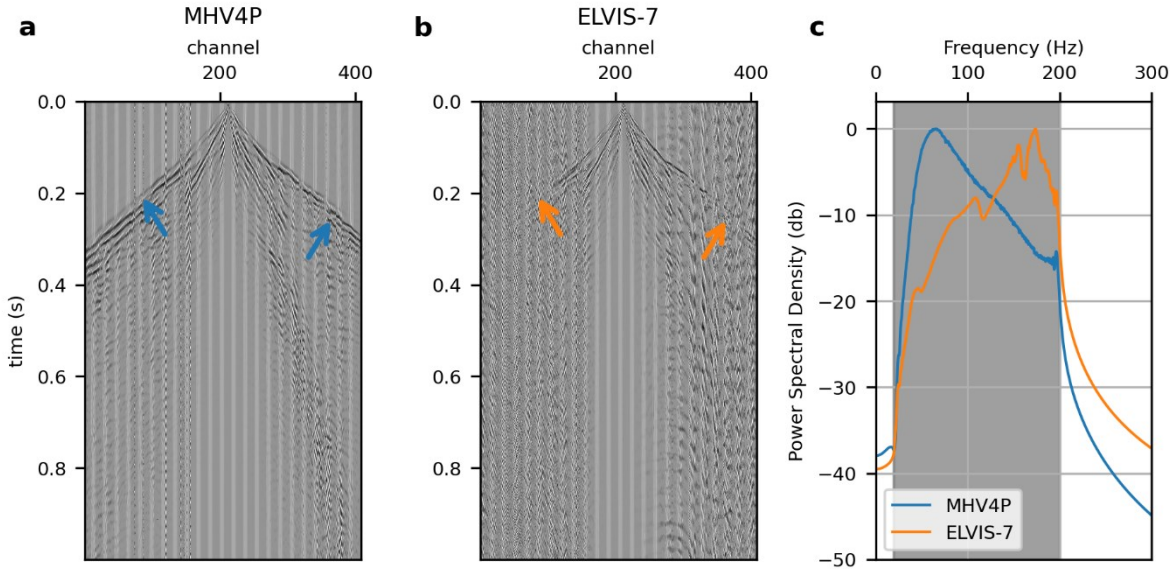

Figure 6: Records of geode- data for neighbouring source locations for vibrators: (a) MHV4P and (b) ELVIS-7, and (c) corresponding power spectral density for vibrators MHV4P (blue) and ELVIS-7 (orange); the sweep frequency range is shaded (gray). The different source strength can be observed by first arrivals that are visible along the entire profile for MHV4P (blue arrows), but not for ELVIS-7 (orange arrows).

Similar to the presented P-wave data, S-wave data show a good data quality (not shown). First arrivals and reflections can be observed on most records.

5.2 HRSR P-wave stacks

The ~~newly~~ newly-acquired data utilizing the vibrator sources and geode-data are able to image the basin base and internal reflectors (Fig. 7). The eastern profile SL-3P shows only horizontal reflectors, similar to the eastern end of SL-2P, and is therefore not shown. On all profiles, we observe horizontal reflectors below 300 m final datum that we interpret as Molasse units (red arrows). These reflectors can also be found at a shallower depth of the eastern part of SL-2P (pink arrows) and on the entire profile SL-3P (not shown). Thus, we infer that in the eastern part of the study site no basin is present, but that it is dominated by Molasse units. We interpret strong reflectors (green arrow) as basal till at the basin base. A dipping reflector within the basin (blue arrows) separates two generations of basin fill, which was

previously unknown. Further internal reflectors are visible as well (purple arrows). The log of borehole 5068_3_A fits the reflectors and supports the interpretation. Unfortunately, the borehole can only support the interpretation for one part of the bipartitioned basin. In the part of SL-2P where we deployed the weaker ELVIS-7 source (between SL-1P and SL-3P in Figs. 7b, d), we observe shallow reflections (orange arrow), but cannot trace the deeper reflectors (yellow arrows) due to less penetration. Therefore, the eastern rim of the basin, that is the transition of the basal basin (green arrows) towards the shallow Molasse reflectors (pink arrows), is not imaged.

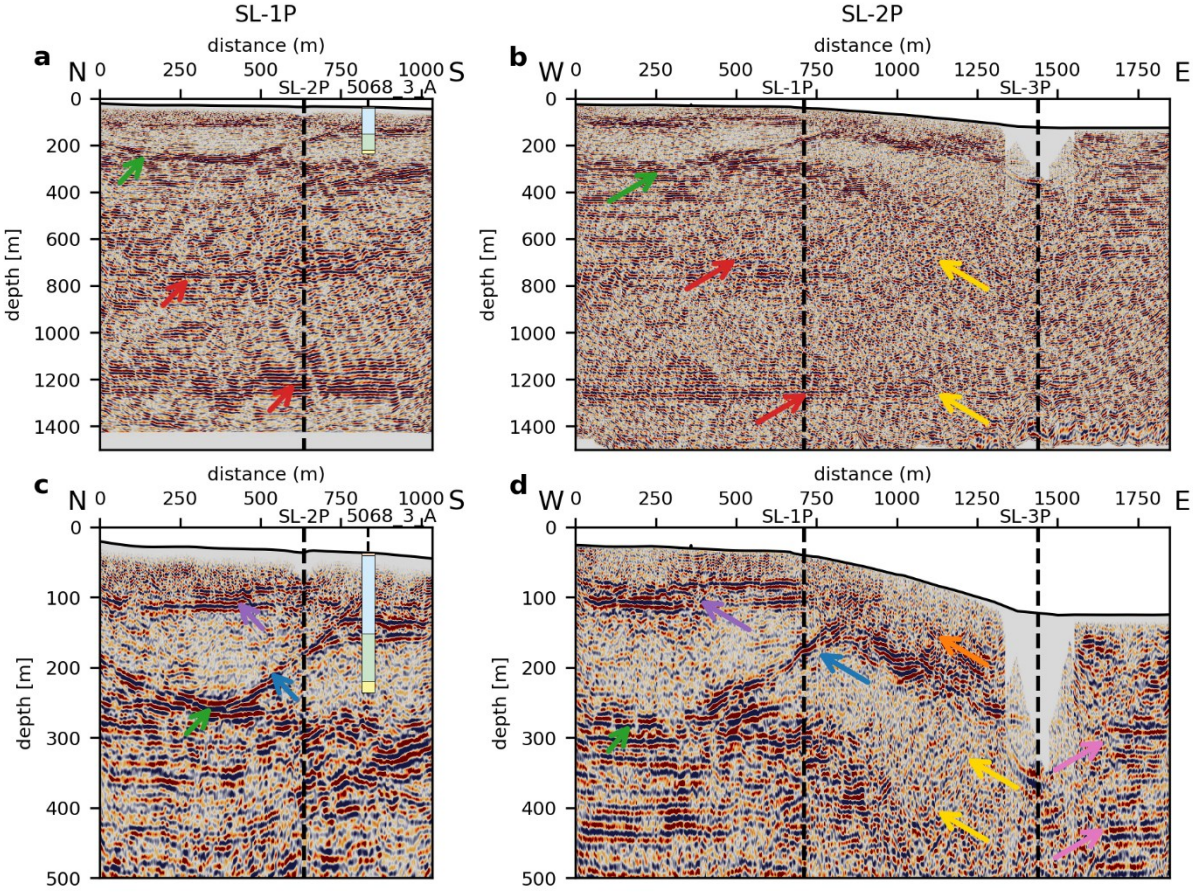

Figure 7: Migrated stacks of (a) SL-1P and (b) SL-2P and ~~zoom~~ close-up ~~to~~ of the first 500 m ~~of~~ in the same profiles with 1.6x vertical exaggeration (c, d). Highlighted by arrows are horizontal Molasse reflectors (red), shallow Molasse reflectors (pink), basin base (green), ~~discontinuity~~ unconformity of bipartitioning (blue), basin internal reflectors (purple), shallow reflectors (orange), and areas with less penetration (yellow). The ELVIS-7 source was deployed on SL-2P only, between SL-1P and SL-3P. The log of borehole 5068_3_A (cf. Fig. 1c) shows the generalized dominant lithology: organic soil (orange), gravel (blue), fines (green), ~~fines (green), sand (orange),~~ and sand (yellow), ~~diamict (gray)~~.

5.3 S-wave stacks and velocities

Stacks of the S-wave data show reflections from a few ms to about 700 ms two-way traveltime, generated by a small-scale ELVIS-7 source. The sections show a similar structural image of the subsurface but with some differences (Figs. 8a, b) compared to the P-wave images (Fig. 7):

1. The reflections are less continuous compared to the P-wave data.
2. S-wave data have less penetration depth than P-wave data.
3. S-wave data show a much higher resolution than the P-wave data.

In detail, we interpret a strong reflection (green arrows) as basal till at the basin base. This reflection shows an undulation that cannot be seen in the P-wave data. A reflection separates the bipartioned basin infills, as seen in the P-wave data (blue arrows). This also exhibits more details than the P-wave data, but is also less continuous. A basin-internal reflection is visible in the S-wave data (purple arrows) that is not present in the P-wave data. In the very shallow part, we observe a continuous reflection (red arrows) with a second reflection directly underneath (pink arrows). Both can be seen in the P-wave data as well, but S-wave data clearly show an overlap of this reflection (pink arrows) that is not visible in the P-wave data. The high resolution of the S-wave data enables detailed interactive velocity picking. S-wave interval velocities (Figs. 8 c, d), calculated from the stacking velocities, show lateral variations that match the overall geology.

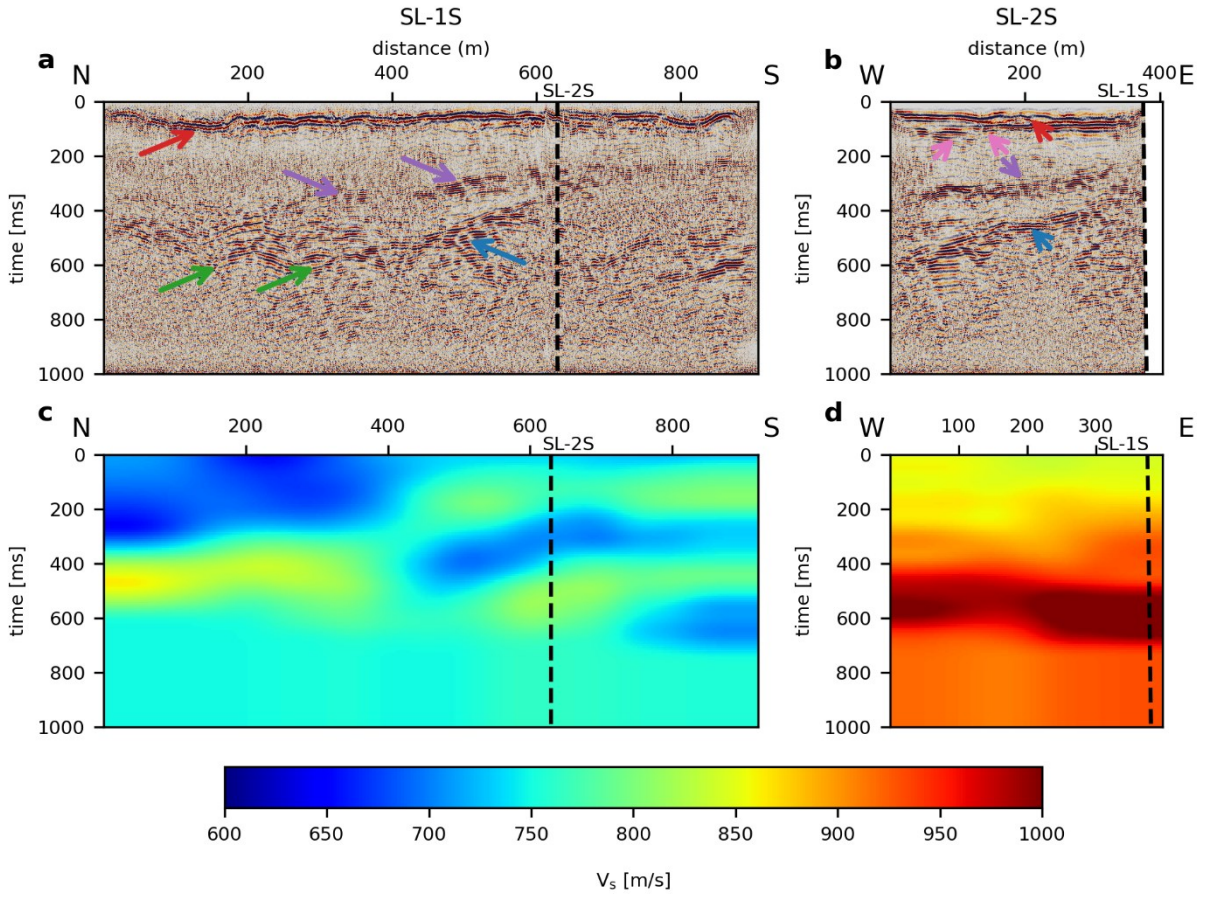

Figure 8: Stacks of (a) SL-1S and (b) the western part of SL-2S and S-wave interval velocities of (c) SL-1S and (d) the western part of SL-2S. Highlighted by arrows are: basin base (green), basin-internal reflectors (purple), intra-basin discontinuity (blue), shallow reflections (red), and shallow discontinuity (pink).

5.4 Full-waveform inversion

The different stages of inversion of the explosive source and geode-data show a successful~~ive~~ updating of the velocity and density distributions from the initial 1-D gradient models to the most detailed model of the last stage, inverting frequencies from 7 Hz to 30 Hz (Fig. 9). Distributions of changes of the last stage compared to the initial model reveal the potential of FWI. The P-wave velocity distribution (Fig. 10a) reveals an undulation in the velocities, which represents small-scale lateral variations in the velocity distribution (red arrows). The velocities~~y results~~ fit the reflectors of the stacked section (Fig. 10b; purple arrow). However, the FWI results contain details up to 30 Hz, while the stacked section contains data up to ~~200~~ 170 Hz. The P-wave velocities of the FWI are in the similar range of the P-wave migration velocity field, derived from HRSR processing (Fig. 10c).

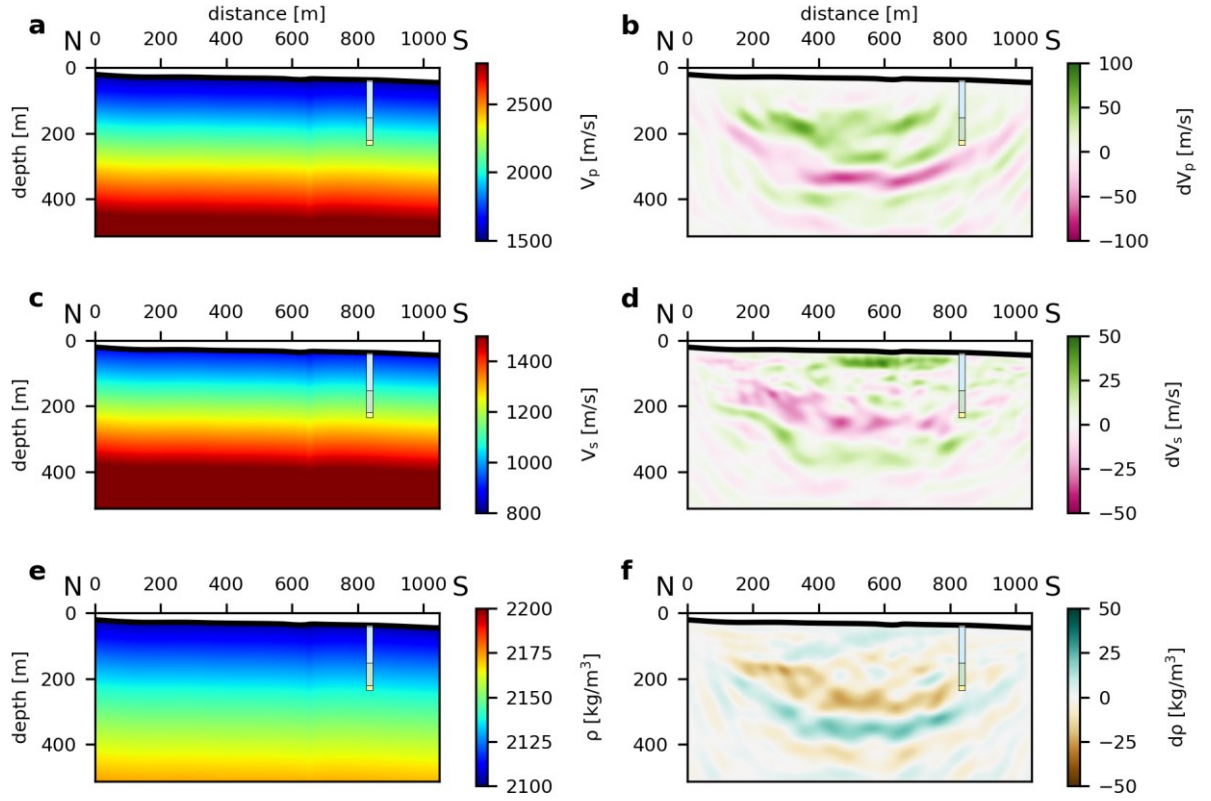
a
b
c
d
e
f
distance [m]
N
S
0
200
400
600
800
1000
depth [m]
V_p [m/s]
dV_p [m/s]
V_s [m/s]
dV_s [m/s]
ρ [kg/m^3]
dρ [kg/m^3]
2500
2000
1500
100
50
−50
−100
1400
1200
1000
800
25
−25
2200
2175
2150
2125
2100

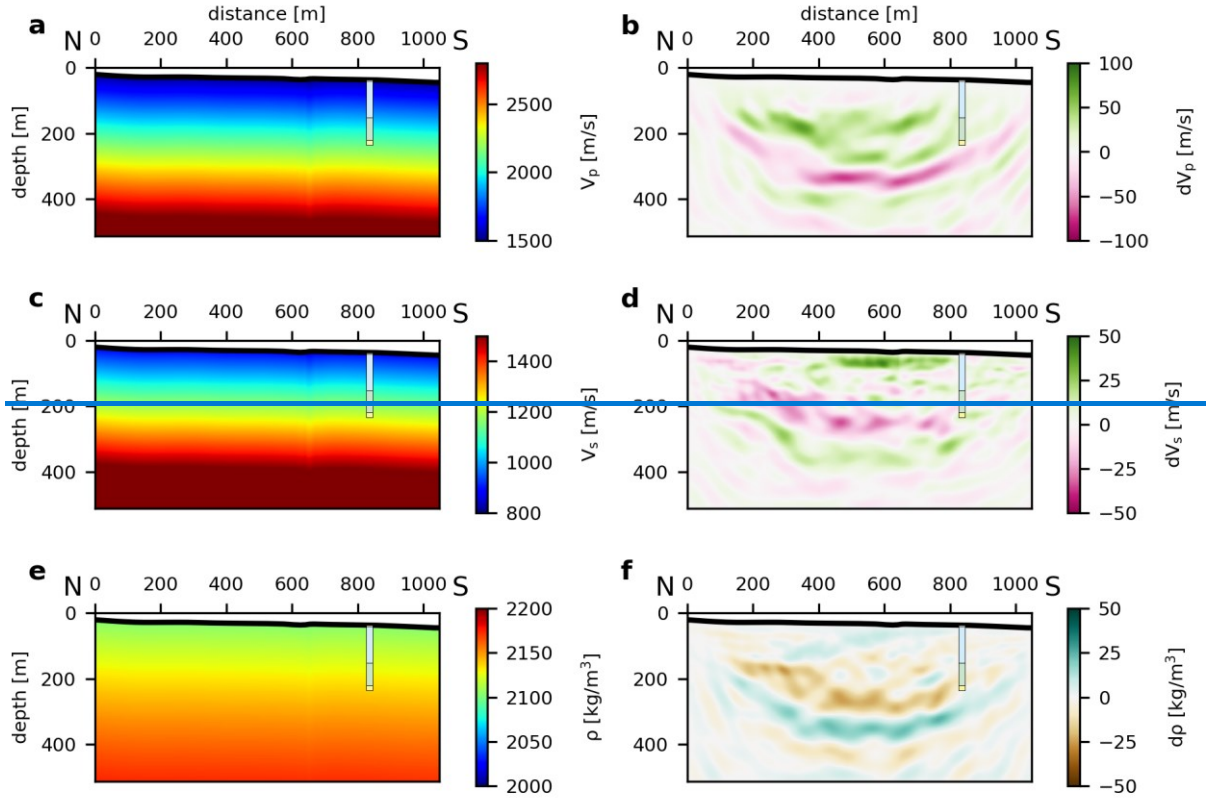

Figure 9: Initial models and changes of the FWI of SL-1P to the initial model for (a, b) P-wave velocity, (c, d) S-wave velocity, and (e, f) density.

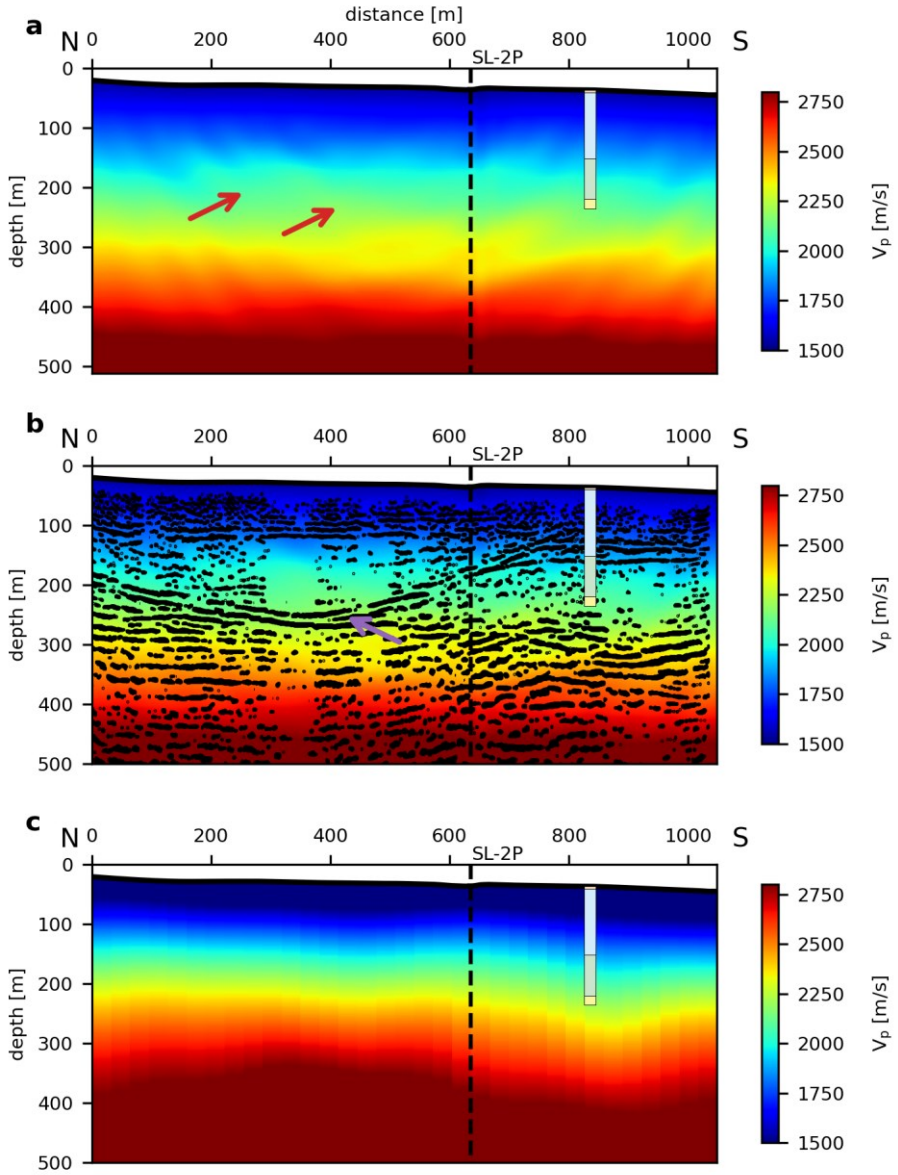

Figure 10: Distributions from (a) the last stage of FWI of SL-1P for P-wave velocity, (b) FWI P-wave velocity with superimposed seismic section ~~superimposed~~, and (c) P-wave velocity from HRSR processing. Highlighted by arrows are: undulations (red arrows) and matching with reflectors in the seismic P-wave section (purple arrow).

6 Discussion

The dataset~~s~~ provide~~s~~ a valuable basis ~~for~~ to develop~~ing~~ the combination of HRSR and FWI for near-surface seismic imaging. The survey parameters were chosen to cover both requirements for HRSR as well as FWI analysis. For HRSR, we used parameters that worked well in Quaternary environments in

the past (e.g., Burschil et al., 2018; Buness et al., 2022). The lower sweep frequency of the vibrator data was determined ~~by~~ from the technical limits of the available MHV4P vibrator ~~MHV4P~~. We chose the upper sweep frequency (200 ~~-~~Hz) due to damping and thus limited benefit of higher frequencies. The charge of the explosives was specified by the blaster. The previous refraction survey of the Bavarian Environment Agency in 2018 used charges of 250 g, but ~~did~~ they were not able to penetrate through the ~~unit of~~ coarse-grained sediments. ~~This was the~~ For this reason, ~~to~~ we increased the charge to 1 kg. The blaster split the 1 kg charge into four 250 g charges per borehole to avoid blowouts.

The lower frequency content of the cube-data is a valuable contribution to the further development of combining HRSR and FWI for the explosive sources. However, the geode-data (20 Hz geophones) show a similar frequency content for the vibrator source as the cube-data (4.5 Hz geophones). Therefore, ~~, so that~~ the effort for ~~in~~ this setup is questionable ~~,~~ if only vibrator sources are available.

A first attempt with explosive sources and the geode-data (20 Hz geophones) shows the potential of FWI to image sedimentary deposits in these environments. The forward-modelled data of the last stage match the field data without cycle skipping (Fig. 11), so that the FWI works sufficiently for the acquired data. However, FWI is often applied to marine data, which often have a better signal-to-noise ratio. ~~Sporadic other~~ L~~l~~and studies ~~also~~ sporadically show the successful application of FWI (e.g., Köhn et al., 2012). On land, ~~horizontally~~ horizontally-polarized S-wave data are often inverted to simplify the inversion problem (e.g., Schwardt et al., 2020; Köhn et al., 2019; Mecking et al., 2021). The penetration depth of the Rayleigh wave is ca. one local S-wavelength (Sheriff and Geldart, 1995). For an average S-wave velocity of 1300 m/s, we get a maximum penetration depth of ~43 m at 30 Hz and ~185 m at 7 Hz. However, as can be seen in the waveform comparison of the records (Fig. 11), the waveforms of first arrival refraction and diving waves ~~are~~ can also be fitted, so the maximum resolution depth extends to ~ 0.5 * maximum offset of the acquisition geometry (~400 - 500 m). The applied staged FWI workflow of this study converges successfully, provides a consistent and physically reasonable solution, and matches the HRSR results.

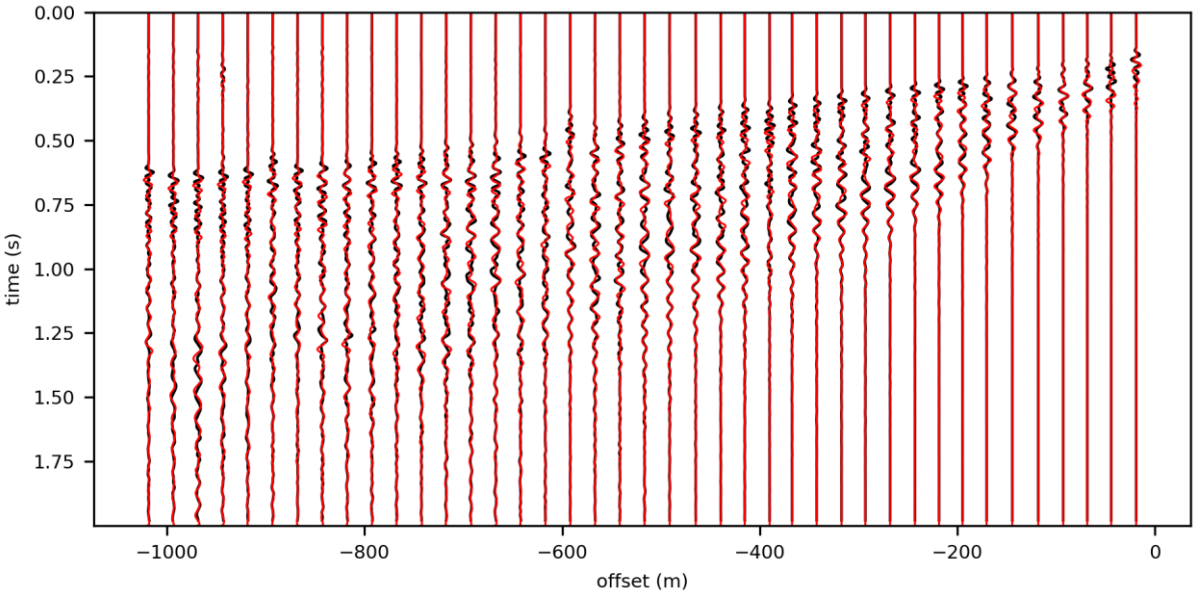

Figure 11: Example of field data (black lines) and forward modelled data of the last stage (red lines) of one record~~s~~. Modelled traces match the field data.

A preliminary interpretation of the P-wave data shows detailed structure within the basin fill. Our interpretation fits the interpretation of the seismic sections, boreholes, and luminescence data by Firla et al. (~~submitted~~2024) at the same site. In general, the sedimentary sequence of glacial and post-glacial deposits is typical for these environments (e.g., Schaller et al., 2023; Schuster et al., 2024). The interpretation suits the reflection pattern that is similar to the seismic facies interpretation of the Tannwald Basin (Burschil et al., 2018), consisting of different lithological units. The S-wave data show very detailed results, imaging the entire basin fill in very good quality, even using the small-scale source. The images show a much higher resolution than those derived from the P-wave data and reveal reflectors that were not observed in the P-wave data. This is in accordance with results from other studies (e.g., Pugin et al., 2009; Brodic et al., 2018; Burschil and Buness, 2020; Pertuz and Malehmir, 2023), even though P-waves ~~are~~ have been commonly used to image Quaternary sediments for decades (e.g., Hunter et al., 1984; Büker et al., 1998; Maries et al., 2017).

7 Conclusions

The acquired datasets demonstrate that they meet the requirements ~~are suitable~~ for the methodical development of combining HRSR and FWI. C~~To meet the prerequisites of each method~~areful integration of complementary source-receiver configurations is essential, with~~, the selection and integration of different source-receiver configurations was essential. While~~ vibrator sources providing ~~with a~~ broad-bandwidth data for HRSR imaging ~~frequency spectrum provide HRSR imaging~~and ~~,~~ explosive sources generating~~e~~ low-frequency signals necessary for FWI. The dense ~~source and~~ receiver spacing enhances~~result~~ both reflection imaging and inversion stability, ~~in a valuable data acquisition~~

scheme. The while autonomous DATA-CUBE³ record the low-frequency receivers can supplement, content of the explosive sources but maydo not significantly improve, the vibrator-based surveys under certain conditions. give a benefit for vibrator sources in this study. Separate analyses of HRSR as well as FWI of different datasets show exhibit that each method provides detailed images in the complex glacially glacially-influenced environment of the overdeepened basin.

The HRSR results images highlight the potential to resolve both the bbasin structures andas well as internal reflectors in of the complex, glacially overdeepened settings, such as the study sitebasin close near to the town Schäftlarn. The We observidentification e horizontal Molasse units and of a previously can delimit the eastern extent of the basin. The internal reflectors reveal a unknown bipartioning of the basin demonstrates the need for HRSR in obtaining a detailed structural characterizationed basin that was previously unknown. Furthermore, S-wave data show provide higher resolution within the basin infill than more details within the basin infill than P-wave data, emphasizing the value of integration both wave types for imaging. This study provides valuable insights for future seismic investigations in glacially overdeepened basins and other heterogeneous geological settings.

Acknowledgments

The project Chatseis is affiliated with the ICDP project Drilling Overdeepened Alpine Valleys (DOVE) and funded by the Deutsche Forschungsgemeinschaft (DFG, German Research Foundation) – 497340281. Particular thanks go to our team at BGR, LIAG, and LfU, especially the blasters Christian Veress and Brian Kröner, during the surveys, as well as the support of the municipality of Schäftlarn and the Monastery Schäftlarn Monastery.

Code/Data availability

Acquired data are available under doi:10.25928/960y-8w55. DENISE Black edition is available at https://github.com/daniel-koehn/DENISE-Black-Edition.

Author contributions

TB managed the project Chatseis, including fieldwork organization, data acquisition, processing of S-waves, seismic interpretation, and preparation of the manuscript. DK organized the DATA-CUBE³ and performed FWI. MK processed the P-wave data. GG organized LIAG fieldwork, and JG organized LfU fieldwork and explosive sources. GF and MF conducted the geological interpretation. All authors contributed to the manuscript.

Competing interests

The authors have no competing interests.

References

Anselmetti, F. S., Bavec, M., Crouzet, C., Fiebig, M., Gabriel, G., Preusser, F., Ravazzi, C., and DOVE scientific team (2022). Drilling Overdeepened Alpine Valleys (ICDP-DOVE): quantifying the age, extent, and environmental impact of Alpine glaciations. Scientific Drilling, 31, 51-70.

Beraus, S., Köhn, D., Bohlen, T., Buness, H., Burschil, T., and Gabriel, G. (2024). High-Resolution Shear Wave Crosshole Full-Waveform Inversion. In Third EAGE Conference on Seismic Inversion (Vol. 2024, No. 1, pp. 1-5). European Association of Geoscientists and Engineers.

Brodic, B., Malehmir, A., Pugin, A., and Maries, G. (2018). Three-component seismic land streamer study of an esker architecture through S-and surface-wave imaging. Geophysics, 83(6), B339-B353.

Brodic, B., Ras, P., de Kunder, R., Drijkoningen, G., and Malehmir, A. (2021). Seismic imaging using an e-vib—A case study analyzing the signal properties of a seismic vibrator driven by electric linear synchronous motors. Geophysics, 86(3), B223-B235.

Buness, H., Tanner, D. C., Burschil, T., Gabriel, G., and Wielandt-Schuster, U. (2022). Cuspate-lobate folding in glacial sediments revealed by a small-scale 3-D seismic survey. Journal of Applied Geophysics, 200, 104614.

Büker, F., Green, A. G., and Horstmeyer, H. (1998). Shallow seismic reflection study of a glaciated valley. Geophysics, 63(4), 1395-1407.

Burschil, T. (2024). Seismic measurements, DOVE site 5068_3 (Schäftlarn), Project Chatseis: Survey report. Federal Institute for Geosciences and Natural Resources, Hannover, Germany, 26p. http://doi.org/10.25928/pet1-6838

Burschil, T., and Buness, H. (2020). S-wave seismic imaging of near-surface sediments using tailored processing strategies. Journal of Applied Geophysics, 173, 103927.

Burschil, T., Buness, H., Tanner, D. C., Wielandt-Schuster, U., Ellwanger, D., and Gabriel, G. (2018). High-resolution reflection seismics reveal the structure and the evolution of the Quaternary glacial Tannwald Basin. Near Surface Geophysics, 16(6), 593-610.

Burschil, T., Buness, H., Leineweber, P., and Polom, U. (2021). Results of Performance Tests of Electrodynamic Vibratory Seismic Sources. In NSG2021 27th European Meeting of Environmental and

Engineering Geophysics (Vol. 2021, No. 1, pp. 1-5). European Association of Geoscientists and Engineers.

Dehnert, A., Lowick, S. E., Preusser, F., Anselmetti, F. S., Drescher-Schneider, R., Graf, H. R., ... and Furrer, H. (2012). Evolution of an overdeepened trough in the northern Alpine Foreland at Niederweningen, Switzerland. Quaternary Science Reviews, 34, 127-145.

Denny, M. D., and Johnson, L. R. (1991). The explosion seismic source function: Models and scaling laws reviewed. Explosion Source Phenomenology, 65, 1-24.

Dokter, E., Köhn, D., Wilken, D., De Nil, D., and Rabbel, W. (2017). Full waveform inversion of SH- and Love-wave data in near-surface prospecting. Geophysical Prospecting, 65(S1), 216-236.

Dragoset, B. (2005). A historical reflection on reflections. The Leading Edge, 24(Supplement), S46-S71.

Ehlers, J., Gibbard,P. L., Hughes, P. D., 2011: Quaternary Glaciations – Extent and Chronology. 1126 pp. Elsevier, Amsterdam.

~~Firla, G., Lüthgens, C., Burschil, T., Neuhuber, S, Schmalfuss, C., Kroemer, E., and Fiebig, M. (submitted). A MIS 8 terrestrial record retrieved from a glacially overdeepened basin in the northern foreland of the European Alps. Submitted to E&G Quaternary Science Journal.~~Firla, G., Lüthgens, C., Preusser, F., and Fiebig, M. (2024). Unravelling the chronology of the infill of glacially overdeepened structures in the northern foreland of the European Alps. Poster, 37th International Geological Congress, Busan, Republic of Korea (South Korea), 25-31 Aug 2024, T2 Quaternary Geology – S3 Current and future directions in Quaternary chronostratigraphy.

Frei, W., Bauer, R., Corboz, P., and Martin, D. (2015). Pitfalls in processing near-surface reflection-seismic data: Beware of static corrections and migration. The Leading Edge, 34(11), 1382-1385.

Hunter, J. A., Pullan, S. E., Burns, R. A., Gagne, R. M., and Good, R. L. (1984). Shallow seismic reflection mapping of the overburden-bedrock interface with the engineering seismograph—Some simple techniques. Geophysics, 49(8), 1381-1385.

Jerz, H. (1979). Das Wolfratshausener Becken: seine glaziale Anlage und Übertiefung. EandG Quaternary Science Journal, 29(1), 63-70.

Jerz, H. (1987). Geologische Karte von Bayern 1:25 000 – 8034 Starnberg Süd. Bayerisches Geologisches Landesamt, Augsburg.

Jerz, H. (1993). Das Eiszeitalter in Bayern – Erdgeschichte, Gesteine, Wasser, Boden. – Geologie von Bayern, 2, Stuttgart.

Köhn, D., De Nil, D., Kurzmann, A., Przebindowska, A., and Bohlen, T. (2012). On the influence of model parametrization in elastic full waveform tomography. Geophysical Journal International, 191(1), 325-345.

Köhn, D., Kurzmann A., De Nil D. and Groos L. (2014). DENISE Black Edition - User manual, available at https://danielkoehnsite.wordpress.com/software/

Köhn, D., Wilken, D., De Nil, D., Wunderlich, T., Rabbel, W., Werther, L., Schmidt, J., Zielhofer, C., and Linzen, S. (2019). Comparison of time-domain SH waveform inversion strategies based on sequential low and bandpass filtered data for improved resolution in near-surface prospecting. Journal of Applied Geophysics, 160, 69-83.

Krohn, C. E. (1984). Geophone ground coupling. Geophysics, 49(6), 722-731.

Lines, L. R., and Clayton, R. W. (1977). A new approach to vibroseis deconvolution. Geophysical prospecting, 25(3), 417-433.

Liu, D. C., and Nocedal, J. (1989). On the limited memory BFGS method for large scale optimization. Mathematical programming, 45(1), 503-528.

Malehmir, A., Saleem, M. U., and Bastani, M. (2013). High-resolution reflection seismic investigations of quick-clay and associated formations at a landslide scar in southwest Sweden. Journal of Applied Geophysics, 92, 84-102.

Manning, T., Ablyazina, D., and Quigley, J. (2019). The nimble node—Million-channel land recording systems have arrived. The Leading Edge, 38(9), 706-714.

Maraio, S., Bruno, P. P. G., Picotti, V., Mair, V., and Brardinoni, F. (2018). High-resolution seismic imaging of debris-flow fans, alluvial valley fills and hosting bedrock geometry in Vinschgau/Val Venosta, Eastern Italian Alps. Journal of Applied Geophysics, 157, 61-72.

Maries, G., Ahokangas, E., Makinen, J., Pasanen, A., and Malehmir, A. (2017). Interlobate esker architecture and related hydrogeological features derived from a combination of high-resolution reflection seismics and refraction tomography, Virttaankangas, southwest Finland. Hydrogeology Journal, 25(3), 829-845.

Mecking, R., Köhn, D., Meinecke, M., and Rabbel, W. (2021). Cavity detection by SH-wave full-waveform inversion—A reflection-focused approach. Geophysics, 86(3), WA123-WA137.

Operto, S., Gholami, Y., Prieux, V., Ribodetti, A., Brossier, R., Métivier, L., and Virieux, J. (2013). A guided tour of multiparameter full-waveform inversion with multicomponent data: From theory to practice. The leading edge, 32(9), 1040-1054.

Ourabah, A., and Chatenay, A. (2022). Unlocking ultra-high-density seismic for CCUS applications by combining nimble nodes and agile source technologies. The Leading Edge, 41(1), 27-33.

Pan, Y., Gao, L., and Bohlen, T. (2019). High-resolution characterization of near-surface structures by surface-wave inversions: from dispersion curve to full waveform. Surveys in Geophysics, 40, 167-195.

Pertuz, T., and Malehmir, A. (2023). Ultrahigh-resolution shear-wave reflection imaging of vertical-component data in a quick-clay prone to landslide area in southwest Sweden. Geophysics, 88(3), B121-B133.

Preusser, F., Reitner, J. M., and Schlüchter, C. (2010). Distribution, geometry, age and origin of overdeepened valleys and basins in the Alps and their foreland. Swiss Journal of Geosciences, 103, 407-426.

Pugin, A. J. M., Pullan, S. E., and Hunter, J. A. (2009). Multicomponent high-resolution seismic reflection profiling. The Leading Edge, 28(10), 1248-1261.

Ren, Z., and Liu, Y. (2015). Elastic full-waveform inversion using the second-generation wavelet and an adaptive-operator-length scheme. Geophysics, 80(4), R155-R173.

Roodaki, A., Janot, L., Peiro, M., Jiang, H., Gao, W., Prigent, H., ... and Kvilhaug, A. (2024). Increasing P-wave and S-wave velocity resolution with FWI—a North Sea shallow water case study. First Break, 42(5), 37-42.

Sallas, J. J. (1984). Seismic vibrator control and the downgoing P-wave. Geophysics, 49(6), 732-740.

Schaller, S., Buechi, M. W., Schuster, B., and Anselmetti, F. S. (2023). Drilling into a deep buried valley (ICDP DOVE): a 252 m long sediment succession from a glacial overdeepening in northwestern Switzerland. Scientific Drilling, 32, 27-42.

Schuster, B., Gegg, L., Schaller, S., Buechi, M. W., Tanner, D. C., Wielandt-Schuster, U., Anselmetti, F., and Preusser, F. (2024). Shaped and filled by the Rhine Glacier: the overdeepened Tannwald Basin in southwestern Germany. Scientific Drilling, 33(2), 191-206.

Schwardt, M., Köhn, D., Wunderlich, T., Wilken, D., Seeliger, M., Schmidts, T., Brücknet, H., Başaran, S., and Rabbel, W. (2020). Characterization of silty to fine-sandy sediments with SH waves: full waveform inversion in comparison with other geophysical methods. Near Surface Geophysics, 18(3), 217-248.

Sheriff, R. E. and Geldart, L. P. (1995). *Exploration seismology*. Second edition, Cambridge University Press.

Singh, B., Malinowski, M., Górszczyk, A., Malehmir, A., Buske, S., Sito, Ł., and Marsden, P. (2022). 3D high-resolution seismic imaging of the iron oxide deposits in Ludvika (Sweden) using full-waveform inversion and reverse time migration. Solid Earth, 13(6), 1065-1085.

Sloan, S. D., Tyler Schwenk, J., and Stevens, R. H. (2016). An example of extreme near-surface variability in shallow seismic reflection data. Interpretation, 4(3), SH1-SH9.

Tanner, D. C., Musmann, P., Wawerzinek, B., Buness, H., Krawczyk, C. M., and Thomas, R. (2015). Salt tectonics of the eastern border of the Leinetal Graben, Lower Saxony, Germany, as deduced from seismic reflection data. Interpretation, 3(3), T169-T13.

Tarantola, A. (1986). A strategy for nonlinear elastic inversion of seismic reflection data. Geophysics, 51(10), 1893-1903.

Ulugergerli, E. U., and Uyanik, O. (2007). Statistical correlations between seismic wave velocities and SPT blow counts and the relative density of soils. Journal of Testing and Evaluation, 35(2), 187-191.

Vigh, D., Cheng, X., Jiao, K., Xu, Z., and Sun, D. (2018). Essential steps for successful full-waveform inversion using land data. In SEG International Exposition and Annual Meeting (pp. SEG-2018). SEG.

Virieux, J., and Operto, S. (2009). An overview of full-waveform inversion in exploration geophysics. Geophysics, 74(6), WCC1-WCC26.

Wadas, S. H., Polom, U., and Krawczyk, C. M. (2016). High-resolution shear-wave seismic reflection as a tool to image near-surface subrosion structures–a case study in Bad Frankenhausen, Germany. Solid Earth, 7(5), 1491-1508.

Wang, Z., Juhlin, C., Lü, Q., Ruan, X., Liu, Z., Yu, C., and Chen, M. (2025). High-resolution seismic reflection surveying to delineate shallow subsurface geological structures in the karst area of Shenzhen, China. Solid Earth, 16(8), 761-773.

Wei, Z., and Phillips, F. (2011). Analysis of vibrator performance at low frequencies. First Break, 29(7).

Zhang, Q., Cheng, S., Chen, W., and Mao, W. (2025). Generating Reliable Initial Velocity Models for Full-waveform Inversion with Well and Structural Constraints. arXiv preprint arXiv:2503.02815.